Soft Matter

Engineering stability, longevity, and miscibility of microtubule-based active fluids

Journal:	*Soft Matter*
Manuscript ID	SM-ART-09-2021-001289.R1
Article Type:	Paper
Date Submitted by the Author:	27-Dec-2021
Complete List of Authors:	Chandrakar, Pooja; Brandeis University Berezney, John; Brandeis University Lemma, Bezia; Harvard University Hishamunda, Bernard; Brandeis University Berry, Angela; Brandeis University Wu, Kun-Ta; Worcester Polytechnic Institute, Physics; Brandeis University, Physics Subramanian, Radhika; Massachusetts General Hospital Chung, Johnson; Brandeis University Needleman, Daniel; Harvard University, Gelles, Jeff; Brandeis University Dogic, Zvonimir; University of California Santa Barbara, Department of Physics

Engineering stability, longevity, and miscibility of microtubule-based active fluids

Pooja Chandrakar [a,g], John Berezney [a], Bezia Lemma [a,b,g], Bernard Hishamunda [a], Angela Berry [a], Kun-Ta Wu [a,c], Radhika Subramanian [d], Johnson Chung [e], Daniel Needleman [b,f,h], Jeff Gelles [e], and Zvonimir Dogic [a,g*]

Microtubule-based active matter provides insight into the self-organization of motile interacting constituents. We describe several formulations of microtubule-based 3D active isotropic fluids. Dynamics of these fluids is powered by three types of kinesin motors: a processive motor, a non-processive motor, and a motor which is permanently linked to a microtubule backbone. Another modification uses a specific microtubule crosslinker to induce bundle formation instead of a non-specific polymer depletant. In comparison to the already established system, each formulation exhibits distinct properties. These developments reveal the temporal stability of nicrotubule-based active fluids while extended their reach and the applicability.

I. Introduction

Studies of active matter are focused on elucidating laws that govern the non-equilibrium dynamics that emerges in collections of motile interacting entities[1-3]. Self-organized active matter phenomena span many length scales, ranging from the coordinated movement of emperor penguins while they huddle, and cell organization assisting the folding of epithelial tissue, to the spontaneous flows observed within biological cells[4-7]. Many biological realizations of active matter consist of complex hard-to-control components, making comparison to theory difficult. Overcoming these obstacles requires experimental model systems where the constituent interactions can be precisely tuned; and consequently, provide a clear pathway for understanding the laws of self-organized active materials.

In this vein, promising model systems are being built from biological materials such as bacteria and cells while others are being assembled from chemically-fuelled Janus swimmers[8, 9]. Each category has its advantages. Active materials consisting of living bacteria and motile eukaryotic cells are energy efficient; thus, they exhibit long-term dynamics, while synthetic elements, such as Janus swimmers, are robustly tuneable. Bridging these two limits are active systems based on cytoskeletal building blocks, such as microtubules (MTs) or actin filaments and associated motor proteins[10-15]. Cytoskeletal active matter combines the best feature of synthetic and living systems. The microscopic dynamics of these systems can be precisely tuned, while energy efficient molecular motors can power long-lived non-equilibrium steady states. These unique features enabled studies of diverse phenomena, ranging from the active nematic liquid crystals and the contractile gels to the collective polar flocks.

Here, we focus on 3D isotropic active fluids, consisting of MTs and molecular motors[16-18]. In such fluids, the extensile MT bundles undergo repeating cascades of kinesin motor-driven extension, buckling, fracturing, and annealing. This network dynamics power persistent spontaneous flows, which can be tuned by varying the concentration of motors, ATP, MTs and depletant. Highly efficient motor proteins are able to sustain non-equilibrium dynamics over several hours. Here we first characterize the temporal stability of conventional microtubule-based active fluids. We then improve the salient properties of these active fluids in multiple ways. First, we power the active fluids by non-processive single-headed kinesin motors instead of the processive double-headed motors. This reduces the motor-induced interference and cross-linking, while improving the temporal stability of the non-equilibrium dynamics. Second, instead of using soluble motor clusters we

[a] The Martin Fisher School of Physics, Brandeis University, Waltham, Massachusetts 02454, USA
[b] School of Engineering and Applied Sciences, Harvard University, Cambridge, Massachusetts 02138, USA
[c] Department of Physics, Worcester Polytechnic Institute, 100 Institute Road, Worcester, Massachusetts 01609, USA
[d] Department of Genetics, HMS and Department of Molecular Biology, Massachusetts General Hospital, Boston, Massachusetts 02114, USA
[e] Department of Biochemistry, Brandeis University, Waltham, Massachusetts 02454, USA
[f] Department of Molecular and Cellular Biology, Harvard University, Cambridge, Massachusetts 02138, USA
[g] Department of Physics, University of California, Santa Barbara, California 93106, USA.
[h] Center for Computational Biology, Flatiron Institute, New York, NY 10010, USA
* Email: zdogic@physics.ucsb.edu

permanently link kinesins onto the MT backbone, thus establishing control over the modes of interactions between two microtubules. Finally, we introduce a depletant-free formulation of isotropic active fluids. We use non-motor MT cross-linkers to bundle filaments; thus, increasing the compatibility of MT based active matter with other filamentous soft materials [19, 20]. The structural modifications developed here can also extended to improve the properties of other MT-based active matter, such as 2D and 3D active nematics[19, 21-24].

II. Building blocks of MT-based active fluids

In this section, we describe the biochemistry of the basic building blocks of the MT-based active fluids, and the rationale for developing new model systems. Previously developed active fluids were assembled from three main components: MTs, kinesin clusters and a bundling agent[16]. MTs are rigid hollow cylinders, polymerized from tubulin dimers, with distinct plus and minus ends[25]. To suppress dynamic instability, MTs were stabilized by non-hydrolysable GTP analogue, GMPCPP (Guanosine 5'-(α,β-methylenetriphosphate)).

The second component of the active fluids is kinesin-1 molecular motors, which transform chemical energy from the ATP hydrolysis to mechanical motion[26]. Each ATP molecule powers a single 8 nm step of a kinesin dimer towards the MT plus end[27]. In previously developed fluids, the kinesin motors were bound into multi-motor clusters that can simultaneously attach to multiple MTs[28], thereby inducing their relative sliding and generating active stresses.

The third component is the non-adsorbing polymer, which induces attractive forces among MTs through the depletion interaction, leading to their bundling, while still allowing the filaments to slide past each other[29-31]. Kinesin clusters powers inter-filament sliding between two aligned, anti-parallel MTs[32]. Bundling enhances inter-filament sliding, since the motor clusters are more likely to bind to multiple filaments in a bundle configuration. The three-component MT-based active fluids were extensively studied[16, 22-24, 33, 34]. However, their lifetime and the temporally stability of the non-equilibrium dynamics have not been quantified.

Previous formulations of active fluids of microtubules and molecular motors used fragments of biotinylated K401 kinesin motors, which are bound into multi-motor clusters with tetrameric streptavidin (**Fig. 1a**). K401 is a kinesin-1 fragment which spontaneously dimerizes[35]. It is a processive motor, which takes ~100 consecutives 8 nm steps, before dissociating from the MT[36]. During this entire sequence, the motor remains firmly linked to the filament. Processive motors can negatively interfere with each other. For example, motility assays showed that increasing motor density leads to a marked slowdown in the MT translocation velocity[37]. A possible reason is that the duration of the actual mechanical step is much smaller than the dwell time between the subsequent steps[38]. When multiple motors are mechanically coupled to the same MT, each stepping motor experiences a hindering load. During its mechanical step kinesin has to work against other motors, which are most likely in the passive dwelling state. Thus, in addition to generating active stress, processive kinesins also increase friction associated with inter-filamentous sliding. Furthermore, while in the dwell state, kinesin motors also act as passive cross-linkers, thus, modifying the network elasticity[39]. Yet, another plausible reason for the slowdown at high motor concentrations is the crowding of motors on the MT surface[40, 41].

Negative interference between the K401 motors decrease the efficiency of inter-filament sliding, especially at high cluster concentrations. To overcome this obstacle, we used the non-processive kinesin K365, a monomeric derivative of kinesin-1, which detaches from the MT after each step (**Fig. 1b**)[35]. Compared to the processive motors, we expected the non-processive K365 to induce less MT cross-linking, and lower negative interference.

Recent theories highlighted the importance of the spatial distribution of motor along a MT in determining the nature of the self-organized active stresses [42, 43]. Different kinesin motors have different preferences for binding along the MT or close to its tip, which are not easily altered. Alternative method for controlling spatial distribution is to permanently affix the kinesin onto the MT with its non-motor-

terminus. To accomplish this, we used human kinesin K560 labeled with the SNAP-tag attached to its C-terminal[44-47]. We labelled the MT with Benzyl-Guanine (BG), which covalently reacts with the SNAP-tag labelled kinesin (**Fig. 1c**).

Other soft materials dissolved in the MT-based active fluid easily incorporate into the extensile bundles, due to the non-specific nature of the depletion interaction. This is an obstacle for making composite active matter. To overcome this hurdle we describe active fluids that are based on the passive MT cross-linker, the protein regulator of cytokinesis 1 (PRC1). PRC1 passively crosslinks the anti-parallel MTs while still allowing for their relative sliding (**Fig. 1d**)[48, 49].

Materials and methods

Kinesin motors and PRC1: K401-BIO-6xHIS (dimeric MW: 110 kDa) and K365-BIO-6xHIS (monomeric MW: 50 kDa) are the 401 and 365 amino acid N-terminal domains derived from the Drosophila melanogaster kinesin and fused to the *E. coli* biotin carboxyl carrier protein. These proteins were expressed and purified from *E. coli* [35, 50]. K365-BIO-6xHIS was derived from K401-BIO-6xHIS by deletion mutation using QuikChange lightning multi-site-directed mutagenesis kit (Agilent Technologies) and contains the first 365 amino acids from the Drosophila kinesin domain of the K410-BIO-6xHIS construct. The chains also contain a six-histidine tag, used for affinity purification with a Ni^{+2}-nitrilotriacetic acid column. K560-SNAPf-6xHIS (dimeric MW: 168 kDa) is a human conventional kinesin construct, comprised of residues 1–560 with a SNAPf-tag and a C-terminal 6-histidine (6xHis) tag [44]. K560-SNAP-6xHIS and K401-BIO-6xHIS are dimeric and processive, whereas K365-BIO-6xHIS is a monomeric and a non-processive kinesin [35, 47].

Biotin on K410-BIO-6xHIS and K365-BIO-6xHIS enables cluster formation through biotin-streptavidin binding. K560-SNAP-6xHIS is modified to include a SNAP-tag, which is a mutant of O6-alkylguanine-DNA alkyltransferase[44, 47]. SNAP-tag is a modified DNA repair protein, which couples covalently to benzylguanine (BG) [46]. All motor proteins were transformed, expressed and purified in Rosetta (DE3) pLysS cells, as previously described [51]. The purified proteins were flash frozen in liquid nitrogen with 36% sucrose, and stored at -80 °C. Biotin on K410-BIO-6xHIS and K365-BIO-6xHIS enables cluster formation through biotin-streptavidin bonding. K560-SNAP-6xHIS is modified to include a SNAP-tag, which is a mutant of O6-alkylguanine-DNA alkyltransferase[44, 47]. SNAP-tag is a DNA repair protein, which binds covalently to benzylguanine (BG) [46]. All motor proteins were transformed, expressed and purified in Rosetta (DE3) pLysS cells, as previously described [51]. The purified proteins were flash frozen in liquid nitrogen with 36% sucrose, and stored at -80 °C.

The full-length PRC1 (MW: 72.5 kDa) and a truncated form of PRC1 were both transformed and expressed in Rosetta BL21(DE3) cells, and purified as previously described [48]. The truncated construct, PRC1-NSΔC, consisting of the first 486 amino acids of the full length PRC1 protein, maintains the dimerization, and concurrently, conserves the rod and MT-binding spectrin domains; but it eliminates the unstructured C-terminal domain, which is susceptible for proteolysis [48]. For brevity, we refer to K365-BIO-6XHIS, K401-BIO-6XHIS and K560-SNAP-6xHIS as K365, K401, K560-SNAP, PRC1 and PRC1-NSΔC respectively.

Kinesin-streptavidin clusters: Dimeric K401 motors have two biotin tags, whereas monomeric K365 has a single tag. K401 and K365 were thawed and incubated with streptavidin (ThermoFisher, 21122, MW: 52.8 kDa) in 1.7:1 biotin to streptavidin ratio, in the presence of DTT. In the case of dimeric kinesin, there was, on average, 0.85 motor per streptavidin molecule. For the K401-streptavidin clusters, 5.7 μL of 6.6 μM streptavidin is mixed with 5 μL of 6.4 μM K401 and 0.5 μL of 5 mM dithiothreitol (DTT) in M2B and incubated on ice for 30 minutes. For the K365-streptavidin clusters, 5.7 μL of 6.6 μM streptavidin is mixed with 3.1 μL of 20 μM K365, 0.5 μL of 5 mM DTT and 1.94 μL of an M2B buffer (80 mM PIPES, 1 mM EGTA, 2 mM $MgCl_2$), and incubated on ice for 30 minutes.

MT and BG-MT polymerization: Tubulin (dimeric MW: 100 kDa) was purified from bovine brains, through two cycles of polymerization-depolymerization in high molarity PIPES (1,4-piperazindiethanesulfonic) buffer[52]. Alexa-Fluor 647-NHS (Invitrogen, A-20006) and BG-GLA-NHS (NEB S9151S) labeled tubulins were prepared as previously described. We did not determine the

BG labelling efficiency. The MT polymerization mixture consisted of the unlabelled tubulins, the 3% fluorophore-labelled tubulin, 1 mM DTT, and 0.6 mM GMPCPP (Jena Biosciences, NU-4056) in M2B buffer. The polymerization was done at 37 °C for 30 minutes, at a tubulin concentration of 80 μM. Subsequently, the polymerization mixture was incubated for 6 hours at room temperature, which resulted in ~1.5 μm long MTs [21]. For the BG-MTs, 6% of the tubulin in the above-mentioned polymerization mixture was BG-labelled.

Efficiency of K560-SNAP bonding reaction: Gel electrophoresis determined the efficiency of the K560-SNAP tubulin labeling reaction (**Fig. 2**). Six different amounts of BG-labeled tubulin were incubated with the same amounts of K560-SNAP, in the presence of 1 mM DTT, at room temperature for 30 minutes. These mixtures were denatured by heating at 100°C, and subsequently loaded for gel-electrophoresis using SDS acrylamide 8% Mops gel (Invitrogen NuPage). The gel electrophoresis data suggests that even though there are saturating numbers of BG-tubulin, only ~30% of K560-SNAP end up binding to the tubulin, for all the concentrations of tubulin proteins (**Fig. 2b**).

Assembly of MT active fluids: The assembly of active fluids required the mixing of the MTs (or BG-labeled-MTs) and a bundling agent (depletant/PRC1/PRC1-NSΔC) with the ATP-consuming motors (K401 or K365 clusters/ K560-SNAP). An ATP regeneration system, comprising of phosphoenol pyruvate (PEP, Beantown Chemical, 129745) and pyruvate kinase/lactate dehydrogenase enzymes (PK/LDH, Sigma, P-0294), retained a constant ATP concentration for the duration of the experiment. In addition, we used an oxygen scavenging system, consisting of glucose, DTT, glucose oxidase (Sigma, G2133) and catalase (Sigma, C40), to minimize the fluorophore photobleaching.

The basic active fluid mixture consisted of 5.5 mM DTT, 3.3 mg/ml glucose, 0.22 mg/ml glucose oxidase, 0.039 mg/ml catalase, 2 mM trolox (Sigma, 238813), 26.67 mM PEP, 1.7 μL of PK/LDH, 3.28 mM of MgCl2 (stock prepared in M2B), 0.016 % tracer particles (Polysciences, 18861), 4.16 % glycerol (functions as a cryoprotectant), 1.42 mM ATP, 2% pluronic (or 25-400 nM of PRC1/PRC1-NSΔC), 13.3 μM MTs, various concentrations of K401/K365 cluster or K560-SNAP.

For K401/K365-based active fluids, a pre-mixture was prepared, consisting of DTT, glucose, glucose oxidase, catalase, Trolox, PEP, pluronic, PK/LDH, $MgCl_2$, fluorescent polystyrene beads, glycerol, freshly polymerized MTs, were added in an Eppendorf tube. The content of this tube was equally divided in 6 aliquots and then varying amount of freshly prepared kinesin-streptavidin clusters and M2B were added to these aliquots. The content of each aliquot was yet again subdivided into small aliquots and flash frozen with liquid nitrogen, and subsequently stored in -80 °C. On the day of the experiment, the frozen sample was thawed, ATP was added to it. This preparation method enhanced the sample reproducibility. Reproducibility was tested by preparing three individual samples, all of which were assembled according to these protocols (**Fig. 3b**)

To assemble K560-SNAP-based active fluids, several reaction mixtures consisting of BG-MT and different amounts of K560-SNAP (final conc. in the active fluid ranges from 5 nM – 150 nM) and 1 mM DTT (in Phosphate-buffered saline) were prepared in different Eppendorf tubes. These mixtures were left to incubate at room temperature for 30 minutes. To remove the K560-SNAP which were not bound to BG-MTs and freely diffusing in the solution, the mixture was centrifuged at 21000 RCF (Eppendorf, Centrifuge 5424 R) for 10 minutes. Next, the pellet was dissolved in a dissociation buffer (pH 7.7) consisting of 350 mM NaCl, 1 mM MgCl2, 1 mM ethylene glycol tetra-acetic acid (EGTA) and 10 mM 4-(2-hydroxyethyl)-1-piperazineethanesulfonic acid (HEPES). It was left to incubate for 2 minutes at room temperature. This step removed the kinesin which were bound to the MTs from non-SNAP end. The dissociation buffer was replaced with M2B by again centrifuging at 21000 RCF and then dissolving the pellet in M2B. Equal volumes of the pre-mixture containing other components of the active fluid were added to each BG-MT-K560-SNAP mixture. The content of each aliquot was yet again subdivided into small aliquots and flash frozen with liquid nitrogen, and subsequently stored in -80 °C. On the day of the experiment, the sample was thawed at room temperature and ATP was added to it.

Importantly, K560-SNAP like K401 and to lesser extend K365 can spontaneously oligomerize and thus could power the active fluid even in the absence of any BG-labeled MTs [53]. This non-specific activity was eliminated using the dissociation buffer and the

centrifugation steps in this protocol which removes the K560-SNAP that are not attached to the BG-MT via SNAP-BG reaction.

For the PRC1 active fluids, freshly polymerized MTs were added to the pre-mixture containing no pluronic, then aliquoted in equal volumes, and finally flash frozen. On the day of the experiment, the frozen aliquot was thawed at room temperature. ATP, and appropriate amounts of PRC1 (or PRC1-NSΔC) and M2B were added to get the required concentrations.

Sample chambers: We used 2 cm×3 mm×100 μm flow channels for our experiments. Glass surfaces were coated with polyacrylamide brush to suppress the surface binding activity of the proteins. To create a flow cell, a spacer is placed between a glass slide (VWR, 25×75×1mm) and a glass coverslip (VWR, 18×18mm, No. 1.5). Spacer material properties influence the sample evolution. Active fluids, made in a channel with a double-sided adhesive tape spacer (Ameritape, 3M9629), decay much faster in comparison to a channel made with a parafilm spacer (Parafilm, PM-996, **Fig. 3a**). To make a flow cell, parafilm was sandwiched between a glass slide and a coverslip, and then heated at 60 °C for a minute. This melted the parafilm, which consequently enabled the coverslip to stick on the glass slide. Finally, the active fluid was loaded in the channel and sealed with an UV glue.

Data acquisition and analysis: To quantify the fluid flows, we doped the fluid with 3 μm passive polystyrene beads, which act as the tracers (**Fig.4**). The buckling of MT bundles induced large-scale flows; as a result, the tracer particles in the solution moved coherently, with approximately similar speeds. All the data were acquired using the fluorescence microscopy technique. A 4x objective (Plan Fluor, NA 0.13), in conjunction with a CCD camera (Andor, Clara), was used to image the tracer particles, as well as the fluorescently labeled MTs. To observe the MT bundles, a confocal microscope (Leica TCS SP8) with a 20x objective (Leica HC Fluotar, NA 0.50) was used. The temperature of the sample chambers was consistently maintained at 20 °C. Particle tracking data were acquired at 10 seconds intervals. A Lagrangian particle tracking algorithm was used to obtain the trajectories of the tracer particles in the XY-plane.

IV. Experimental results

First, we quantified the temporal behavior of previously studied active fluids, powered by the processive K401 clusters (**Fig. 5a**). We measured the time evolution of the average in-plane speed - denoted as $\langle |v_{xy}| \rangle$ - of the tracer particles. The system self-organized on a timescale that was determined by the motor concentration. Upon achieving the maximum speed active fluid dynamics slowly slowed down, and after a well-defined time ceased rapidly. After the dynamics ceased, doping an active fluid with more ATP regenerating components recovered the activity. This suggests that the active fluid lifetimes are dictated by the available energy resources.

The dependence of the maximum speed – denoted as $|\mathrm{v_{max}}|$ - on the kinesin cluster concentration was extracted from the speed-time plots (**Fig. 5b**). There is an optimum motor concentration of 50 nM that maximized the system dynamics; increasing the motor cluster up to 50 nM sped up the dynamics. At higher motor concentrations, the active fluid dynamics slowed down markedly. Motor cluster concentration affected other properties of the active fluids. For example, at low concentration (5 nM) the system attained the maximum speed after 3 hours, whereas there was no detectable build-up time at higher motor concentrations. Furthermore, increasing the motor concentration resulted in shorter fluid lifetimes (**Fig. 5b**).

We also characterized the structure of the autonomous flows by measuring the spatial velocity-velocity correlation length (denoted as $\frac{\langle \mathrm{v(r).v(r+\Delta r)} \rangle}{\langle \mathrm{v(r).v(r)} \rangle}$), which decayed exponentially as $\mathrm{e}^{\frac{-\Delta r}{\lambda}}$ (**Fig. 5c**). Below ~40 μm length-scale our measurements were unreliable, owing to the ~50 μm depth of focus of the objective (Nikon, 4× Plan Fluor, NA 0.13). The velocity-velocity correlation curves, plotted at different time points (data averaged over 1-hour interval), did not collapse on each other; instead, they decreased (**Fig. 5d**). Such a decaying trend, in conjunction with the decreasing mean speed of autonomous flows, suggests that the structure of K401-based active fluids changed over time.

Next, we studied active fluids powered by clusters of the non-processive K365 motors (**Fig. 6a**). At 20 nM cluster concentration, the system dynamics slowly increased over time, attaining its maximum speed after ~3 hours. At higher concentrations, there was no detectable build-up of speed: the

maximum self-organized dynamics appeared instantaneously. Once the system attained the maximum speed, the velocity plateau remained flat in comparison to K401-based fluids. Such steady-state dynamics persisted, until ceasing due to the ATP depletion. The maximum fluid speed increased with increasing K365 cluster concentration, and it plateaued above 75 nM (**Fig. 6b**). Furthermore, all the correlation curves collapsed on each other, and the correlation lengths remained invariant over the sample lifetime (**Fig. 6c, d**). Taken together this data demonstrates that K365 active fluids maintain more constant dynamics, when compared to the K401 system. Like the K401 system, increasing K365 cluster concentrations, shortens the fluid lifetimes.

Next, we studied active fluids powered by K560-SNAP motors. Unlike freely diffusing K401 or K365 motor clusters, K560-SNAP was covalently bonded to BG-labeled MT backbone. Increasing the K560-SNAP concentrations shortened the lifetimes of these active fluids (**Fig. 7a**). The K560-SNAP active fluids did not maintain steady speeds over the sample lifetime, instead they exhibited a significant decay for motor concentrations higher than 25 nM. The reason for this large drop off is not clear. The maximal fluid speed increased with increasing motor cluster concentration, and plateaued at higher values (**Fig. 7b**). Similar to the K401 system, the velocity correlation functions, at different times did not collapse on each other; and λ decreased with time (**Fig. 7c, d**).

In the final active fluid formulation, we replaced the depletion agent with a specific MT crosslinker: protein regulator of cytokinesis (PRC1)[48]. The average speed over time had a similar form to the other systems: first, it decayed slowly, but after a well-defined time, it ceased rapidly (**Fig. 8**). System dynamics was maximal for 100 nM PRC1 concentration, but for these conditions speeds exhibited largest decay in speed with increasing sample time. Decreasing the cross-linker concentration below 100 nM decreased the fluid speed, which might be due to the absence of sufficient cross-linkers to bundle the MTs. Overall the sample to sample reproducibility of the PRC1-based fluids was low, which might be related to the degradation of the PRC1, which is susceptible to proteolysis.

To increase the stability of PRC1 based active fluids we also studied PRC1-NSΔC, which is more robust against degradation due to the deleted non-structured C-terminus[48]. This data was similar to the full-length protein: 100 nM concentrations of PRC1-NSΔC optimized the maximum speed of the active fluid (**Fig. 9a**). Notably, the fluid velocities in the PRC1-NSΔC fluids were significantly higher when compoared to those measured for the full-length protein Additionally, higher concentrations of PRC1-NSΔC, although relatively slow, displayed nearly time-invariant mean velocities. Finally, in contrast to the full length crosslinker, PRC1-NSΔC fluids had lifetimes that scaled nearly linearly with the concentration of the cross-linker. There is a qualitative correspondence between the time evolution of the active fluid speed and the variations of the microtubule network structure (**Fig. 9b**). For example, 25 and 100 nM crosslinker network start with very large initial velocity but the velocity decays quite rapidly to zero. Equivalently, the network structure also evolved quite strongly over time. In comparison, at 400 nM crosslinker concentration the fluid speed is nearly constant over time and equivalently the network structure has qualitatively the saem appearance at different time points.

V. Discussion

We quantified the temporal stability of K401 fluids, finding that the average speed of their autonomous flows and their structural correlation length decreased over the sample lifetime. Furthermore, increasing the motor concentration beyond a threshold value reduced the flow speed, presumably due to motor interference [37]. These findings identify several drawbacks of the conventional K401-based active fluids.

Motivated by the deficiencies of the K401-based system, we characterized active fluids that are powered by the non-processive K365 motors, finding superior properties. The average speed and the spatial correlation length of K365 fluids remained nearly constant over the sample lifetime. Furthermore, unlike the K401 system, the K365 active fluids did not exhibit a decrease in the system speed at high clusters concentrations. This might be due to the reduced interference between the non-processive K365 motors. These developments pave the way for quantifying the dynamics of the 2D active nematic liquid crystals powered by K365 motors. Recent experiments suggested that, at low ATP concentrations, the conventional K401 motors significantly modify the liquid crystal elastic

constants [39, 54]. K365-based active nematics might alleviate these effects.

Efficient K365 based inter-filament sliding raises several questions. First, the speed of the K365 fluids is comparable to the conventional K401 systems. This contrasts with the motility experiments, where the single-headed kinesin-generated velocities were significantly smaller than those of the double-headed motors [35, 55, 56]. Second, in the motility assays single-headed motors generated motion only when multiple motors were interacting with a MT simultaneously. A minimum of 4 to 6 motors were required to generate any motion. We observed significant dynamics at cluster concentrations as low as 20 nM. Under these conditions, there are only about four motor clusters per MT, similar to the number of single-headed motors that need to be engaged with a MT. However, in a motility assay the motors are permanently attached to the solid surface: each step imparts force on the sliding MT. In active fluids, clusters need to be engaged with both the MTs to generate sliding motion. However, the low duty ratio of single-headed motors reduces the probability of such occurrences. These inconsistencies suggest insufficient understanding of how the single-headed motors generate MT sliding.

Recent, single molecule experiments and associated analysis suggested that the rate of kinesin unbinding from MT is dependent on both the direction and the magnitude of the applied force load [57, 58]. In particular, loads along the MT and opposing the kinesin stepping can dramatically increase the lifetime of the kinesin-MT bond. It is possible that non-processive motors experience such loads within bundles, and these loads effectively increases the kinesin duty ratio. Indeed, experiments suggested that kinesin-1 motors in active nematics are under a significant loads that are directed along the direction of MT alignment [59].

We showed that linking the motor proteins to the MT backbone leads to long-lived extensile active fluids. This system allows motors to be spatially patterned along the MT backbone, by assembling segmented microtubules[60]. Control over the distribution of motors to the plus or minus end of the microtubules could provide insight into mechanism by which molecular motors generate dipolar extensile/contractile active stresses [61].

In conventional microtubule-based active matter, the filaments are bundled with the depletant polymers. However, excluded-volume based depletion forces are non-specific, thus limiting the compatibility of active fluids with other soft materials. To overcome this obstacle, we used PRC1 as a cross-linking agent specific to the anti-parallel MTs. PRC1-based active fluids open the door for assembling composite active systems. Given PRC1's specific preference for the MTs, the secondary material should not interfere with the MT bundling. PRC1-based active fluids enable assembly of composite systems, such as 3D active nematics, wherein the dilute MT fluid generates active stresses, which subsequently drive the passive component away from equilibrium[19, 20].

The active fluid lifetime is determined by the amount of the chemical fuel or equivalently the total ATP and PEP concentration. Therefore, sample lifetime measurements provide insight into the rate of ATP hydrolysis. We estimate the hydrolysis rate of K401 active fluids by dividing the total available ATP (plus PEP) by the sample lifetime and the concentration of molecular motors. The ATP hydrolysis rate obtained in such a way is noisy, but consistently ranges from 21-37 ATPs/s per motor. There is also no discernible trend of ATP hydrolysis on the motor concentration. It is insightful to compare this estimate to other measurement of ATP hydrolysis. Our measurement closely agrees with the rate estimated from the calorimetry of bulk active gels[62]. It is also possible to estimate ATP hydrolysis rate from the motility assay experiments, since each 8 nm step is fueled by hydrolysis of a single ATP[27]. Motility indicate, at saturating ATP concentration in the absence of external load kinesin-1 steps at ~680 nm/s taking 8 nm steps[27, 37, 63], which yields about 80 ATPs per second. Finally, ATP hydrolysis rate was also measured in conventional bulk biochemical assays[64] These measurement, which studied non-cluster bound kinesin motors, estimated that hydrolyzes ~20 ATPs per second. Our measurements are on the low end of this spectrum. Importantly there are possible significant variations between different experiments that are not accounted for. For example, there could be different fraction of motors that are engaged with microtubules and different average force loads could decrease the velocity of kinesin and their hydrolysis rate[63, 65].

In summary, we described several formulations of active fluids that are powered by distinct microscopic units, yet all exhibit qualitatively same large-scale dynamics. In particular, our findings demonstrate the advantages of using clusters of non-processive motors to maintain steady dynamics. They also demonstrate a depletion-free method of assembling active fluids, which is useful for assembly of the active composites. It would be of considerable interest to study how the knowledge generated from our studies of 3D isotropic active fluids is transferred to other manifestations of MT-based active matter, such as 2D active nematic. Our studies also demonstrate the challenge of developing multiscale understanding of active fluids, where the large scale dynamics can be described in term of properties of

Conflicts of interests: There are no conflicts to declare.

Author Contributions: P.C. and J.B. performed experiments and analyzed data. B.L., R.S. and D.N. developed and purified PRC1. J.G. and J.C. developed K365-bio-H6 and protein purification protocols. A.B., B.H. and K-T.W. performed preliminary experiments. P.C. and Z.D. prepared the manuscript with critical input from all authors.

Acknowledgements: This study was primarily supported by the Department of Energy of Basic Energy Sciences, through award DE-SC0019733. Design of the proteins for this work were supported by Brandeis MRSEC, through grant NSF-MRSEC-2011846. We also acknowledge the use of a MRSEC optical and biosynthesis facility supported by NSF-MRSEC-2011846. The K560-SNAP was a gift from S. L. Reck-Peterson.

References:

1. S. Ramaswamy, *Annual Review of Condensed Matter Physics*, 2010, **1**, 323-345.
2. M. C. Marchetti, J. F. Joanny, S. Ramaswamy, T. B. Liverpool, J. Prost, M. Rao and R. A. Simha, *Reviews of Modern Physics*, 2013, **85**, 1143-1189.
3. D. Needleman and Z. Dogic, *Nature Reviews Materials*, 2017, **2**, 17048.
4. Y. H. Tee, T. Shemesh, V. Thiagarajan, R. F. Hariadi, K. L. Anderson, C. Page, N. Volkmann, D. Hanein, S. Sivaramakrishnan and M. M. Kozlov, *Nature cell biology*, 2015, **17**, 445.
5. D. P. Zitterbart, B. Wienecke, J. P. Butler and B. Fabry, *PLOS ONE*, 2011, **6**, e20260.
6. B. He, K. Doubrovinski, O. Polyakov and E. Wieschaus, *Nature*, 2014, **508**, 392-396.
7. S. J. Streichan, M. F. Lefebvre, N. Noll, E. F. Wieschaus and B. I. Shraiman, *eLife*, 2018, **7**, e27454.
8. J. Palacci, S. Sacanna, A. P. Steinberg, D. J. Pine and P. M. Chaikin, *Science*, 2013, **339**, 936.
9. I. Theurkauff, C. Cottin-Bizonne, J. Palacci, C. Ybert and L. Bocquet, *Physical review letters*, 2012, **108**, 268303.
10. T. Surrey, F. Nédélec, S. Leibler and E. Karsenti, *Science*, 2001, **292**, 1167.
11. P. J. Foster, S. Fürthauer, M. J. Shelley and D. J. Needleman, *eLife*, 2015, **4**, e10837.
12. S. Köhler, V. Schaller and A. R. Bausch, *Nature Materials*, 2011, **10**, 462.
13. V. Schaller, C. Weber, C. Semmrich, E. Frey and A. R. Bausch, *Nature*, 2010, **467**, 73.
14. G. H. Koenderink, Z. Dogic, F. Nakamura, P. M. Bendix, F. C. MacKintosh, J. H. Hartwig, T. P. Stossel and D. A. Weitz, *Proceedings of the National Academy of Sciences*, 2009, **106**, 15192-15197.
15. M. P. Murrell and M. L. Gardel, *Proceedings of the National Academy of Sciences*, 2012, **109**, 20820-20825.
16. T. Sanchez, D. T. N. Chen, S. J. DeCamp, M. Heymann and Z. Dogic, *Nature*, 2012, **491**, 431.
17. K.-T. Wu, J. B. Hishamunda, D. T. N. Chen, S. J. DeCamp, Y.-W. Chang, A. Fernández-Nieves, S. Fraden and Z. Dogic, *Science*, 2017, **355**.
18. G. Henkin, S. J. DeCamp, D. T. N. Chen, T. Sanchez and Z. Dogic, *Philosophical Transactions of the Royal Society A: Mathematical, Physical and Engineering Sciences*, 2014, **372**.
19. G. Duclos, R. Adkins, D. Banerjee, M. S. Peterson, M. Varghese, I. Kolvin, A. Baskaran, R. A. Pelcovits, T. R. Powers and A. Baskaran, *Science*, 2020, **367**, 1120-1124.
20. J. Berezney, B. L. Goode, S. Fraden and Z. Dogic, *arXiv preprint arXiv:2110.00166*, 2021.
21. S. J. DeCamp, G. S. Redner, A. Baskaran, M. F. Hagan and Z. Dogic, *Nature Materials*, 2015, **14**, 1110.
22. P. Guillamat, J. Ignés-Mullol and F. Sagués, *Proceedings of the National Academy of Sciences*, 2016, **113**, 5498-5502.
23. P. W. Ellis, D. J. Pearce, Y.-W. Chang, G. Goldsztein, L. Giomi and A. Fernandez-Nieves, *Nature Physics*, 2018, **14**, 85.
24. A. J. Tan, E. Roberts, S. A. Smith, U. A. Olvera, J. Arteaga, S. Fortini, K. A. Mitchell and L. S. Hirst, *Nature Physics*, 2019, **15**, 1033-1039.
25. E. Nogales, M. Whittaker, R. A. Milligan and K. H. Downing, *Cell*, 1999, **96**, 79-88.
26. R. D. Vale, *Cell*, 2003, **112**, 467-480.
27. M. J. Schnitzer and S. M. Block, *Nature*, 1997, **388**, 386.
28. F. Nedelec, T. Surrey, A. C. Maggs and S. Leibler, *Nature*, 1997, **389**, 305-308.

29. D. J. Needleman, M. A. Ojeda-Lopez, U. Raviv, K. Ewert, J. B. Jones, H. P. Miller, L. Wilson and C. R. Safinya, *Physical review letters*, 2004, **93**, 198104.
30. F. Hilitski, A. R. Ward, L. Cajamarca, M. F. Hagan, G. M. Grason and Z. Dogic, *Physical Review Letters*, 2015, **114**, 138102.
31. A. Ward, F. Hilitski, W. Schwenger, D. Welch, A. Lau, V. Vitelli, L. Mahadevan and Z. Dogic, *Nature materials*, 2015, **14**, 583.
32. L. M. Lemma, M. M. Norton, S. J. DeCamp, S. A. Aghvami, S. Fraden, M. F. Hagan and Z. Dogic, *arXiv preprint arXiv:2006.15184*, 2020.
33. F. C. Keber, E. Loiseau, T. Sanchez, S. J. DeCamp, L. Giomi, M. J. Bowick, M. C. Marchetti, Z. Dogic and A. R. Bausch, *Science*, 2014, **345**, 1135-1139.
34. A. Senoussi, S. Kashida, R. Voituriez, J.-C. Galas, A. Maitra and A. Estevez-Torres, *Proceedings of the National Academy of Sciences*, 2019, **116**, 22464-22470.
35. E. C. Young, H. K. Mahtani and J. Gelles, *Biochemistry*, 1998, **37**, 3467-3479.
36. K. S. Thorn, J. A. Ubersax and R. D. Vale, *The Journal of cell biology*, 2000, **151**, 1093-1100.
37. P. Bieling, I. A. Telley, J. Piehler and T. Surrey, *EMBO reports*, 2008, **9**, 1121.
38. N. J. Carter and R. Cross, *Nature*, 2005, **435**, 308-312.
39. D. A. Gagnon, C. Dessi, J. P. Berezney, R. Boros, D. T.-N. Chen, Z. Dogic and D. L. Blair, *Physical Review Letters*, 2020, **125**, 178003.
40. A. Seitz and T. Surrey, *The EMBO journal*, 2006, **25**, 267-277.
41. C. Leduc, K. Padberg-Gehle, V. Varga, D. Helbing, S. Diez and J. Howard, *Proceedings of the National Academy of Sciences*, 2012, **109**, 6100-6105.
42. M. Lenz, *eLife*, 2020, **9**, e51751.
43. B. Lemma, N. P. Mitchell, R. Subramanian, D. J. Needleman and Z. Dogic, *arXiv preprint arXiv:2107.12281*, 2021.
44. N. D. Derr, B. S. Goodman, R. Jungmann, A. E. Leschziner, W. M. Shih and S. L. Reck-Peterson, *Science*, 2012, **338**, 662-665.
45. A. Keppler, M. Kindermann, S. Gendreizig, H. Pick, H. Vogel and K. Johnsson, *Methods*, 2004, **32**, 437-444.
46. A. Keppler, H. Pick, C. Arrivoli, H. Vogel and K. Johnsson, *Proceedings of the National Academy of Sciences of the United States of America*, 2004, **101**, 9955.
47. R. B. Case, D. W. Pierce, N. Hom-Booher, C. L. Hart and R. D. Vale, *Cell*, 1997, **90**, 959-966.
48. R. Subramanian, E. M. Wilson-Kubalek, C. P. Arthur, M. J. Bick, E. A. Campbell, S. A. Darst, R. A. Milligan and T. M. Kapoor, *Cell*, 2010, **142**, 433-443.
49. E. H. Kellogg, S. Howes, S.-C. Ti, E. Ramírez-Aportela, T. M. Kapoor, P. Chacón and E. Nogales, *Proceedings of the National Academy of Sciences*, 2016, **113**, 9430.
50. D. S. Martin, R. Fathi, T. J. Mitchison and J. Gelles, *Proceedings of the National Academy of Sciences*, 2010, **107**, 5453.
51. R. F. Douglas S. martin, Timothi J. Mitchison, Jeff Gelles, *PNAS*, 2010, 5453-5458.
52. A. V. P. M. Castoldi, *Protein Expression and Purification*, 2003, 83-88.
53. A. M. Tayar, M. F. Hagan and Z. Dogic, *Proceedings of the National Academy of Sciences*, 2021, **118**, e2102873118.
54. L. M. Lemma, S. J. DeCamp, Z. You, L. Giomi and Z. Dogic, *Soft matter*, 2019, **15**, 3264-3272.
55. W. O. Hancock and J. Howard, *The Journal of cell biology*, 1998, **140**, 1395-1405.
56. S. M. Block, *The Journal of cell biology*, 1998, **140**, 1281-1284.
57. J. O. Andreasson, B. Milic, G.-Y. Chen, N. R. Guydosh, W. O. Hancock and S. M. Block, *Elife*, 2015, **4**, e07403.
58. H. Khataee and J. Howard, *Physical review letters*, 2019, **122**, 188101.
59. A. M. Tayar, M. F. Hagan and Z. Dogic, *Proceedings of the National Academy of Sciences*, 2021, **118**.
60. A. Hyman, *Journal of Cell Science*, 1991, **1991**, 125-127.
61. S. Fürthauer, D. J. Needleman and M. J. Shelley, *New Journal of Physics*, 2021, **23**, 013012.
62. P. J. Foster, J. Bae, B. Lemma, J. Zheng, P. Chandrakar, Z. Dogic, D. J. Needleman and J. J. Vlassak, *Recently submitted for publication*, 2021.
63. K. Visscher, M. J. Schnitzer and S. M. Block, *Nature*, 1999, **400**, 184-189.
64. C. M. Farrell, A. T. Mackey, L. M. Klumpp and S. P. Gilbert, *Journal of Biological Chemistry*, 2002, **277**, 17079-17087.
65. K. Visscher, M. J. Schnitzer and S. M. Block, *Nature*, 1999, **400**, 184-189.

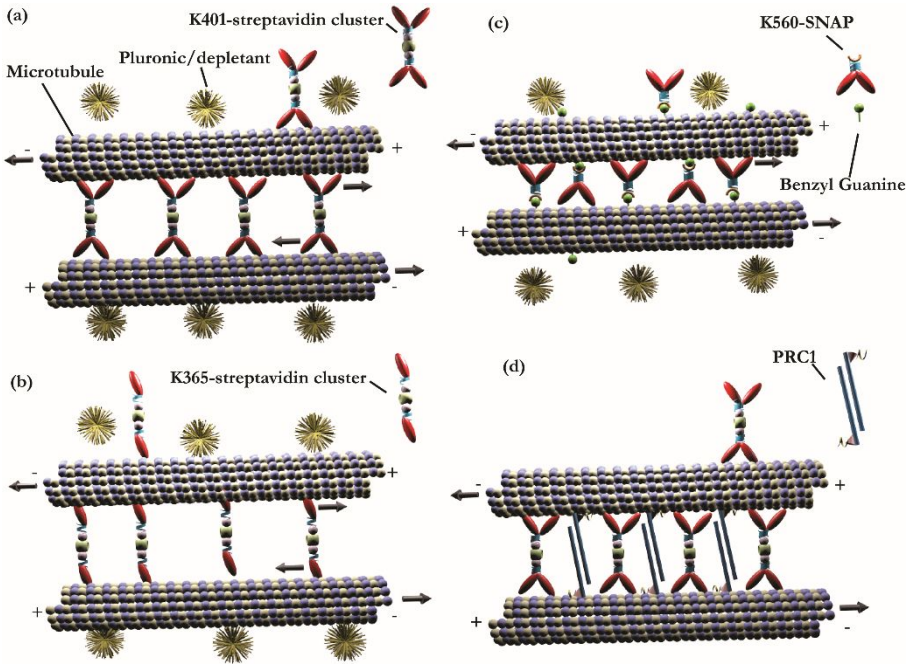

Fig. 1. Microscopic building blocks for four types of active fluids. (a) Previously studied active fluids consisted of MTs, clusters of double-headed processive kinesin motors (K401) and a depleting agent. **(b)** Modified active fluids powered by clusters of single-headed non-processive kinesin motors (K365). **(c)** Modified active fluids powered by double-headed processive kinesin K560-SNAP that is covalently bonded to the MT. **(d**) Modified active fluids in which non-specific depletion agent (pluronic) was replaced by PRC1, a protein that crosslinks anti-parallel MTs.

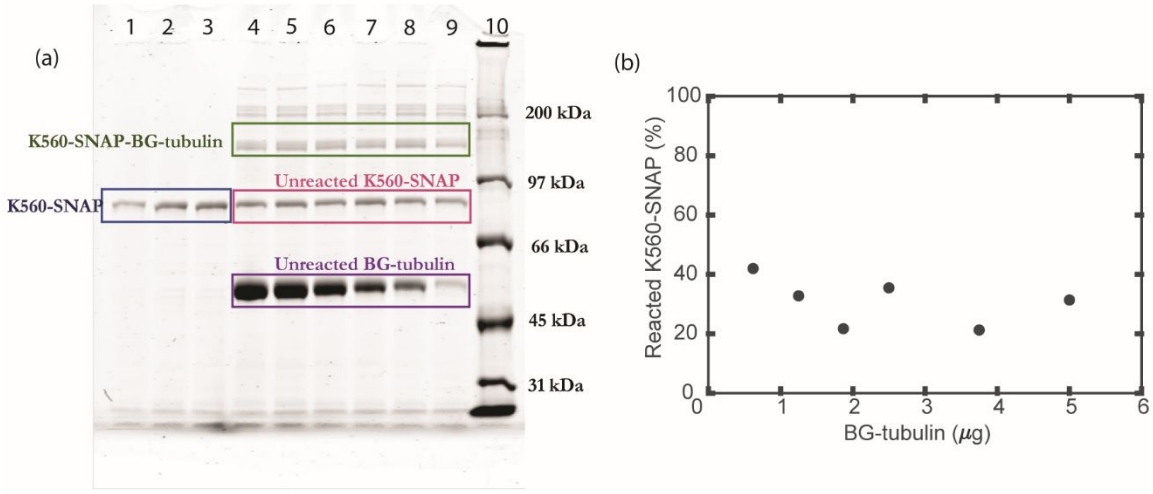

Fig. 2. Efficiency of the SNAP-based bonding reaction estimated by gel electrophoresis (a) Lanes 1-3 contain 0.87, 1.31, 1.75 μg of K560-SNAP, respectively. Lanes 4-9 contain 1.75 μg of K560-SNAP incubated with decreasing amounts of BG tubulin, 5, 3.75, 2.5, 1.87, 1.25 and 0.62 μg, respectively. Lane 10 contains the standard, SDS-broad range protein (Bio-Rad, 161-0317). The bands at 50 kDa are unreacted tubulin monomers; the bands at 84 kDa correspond to unreacted K560-SNAP, and the band at ~134 kDa

correspond to linked K560-SNAP-BG-tubulin complex. All the bands at and above 200 kDa are associated with protein structures that are not fully understood. **(b)** Using the intensity versus amount of K560-SNAP from lane 1-3, we interpolated the amount of unreacted K560-SNAP in lanes 4-9. The difference between the total amount of K560-SNAP added in the reaction mixture and the estimated, unreacted K560-SNAP was inferred as the amount of K560-SNAP that reacted with BG-tubulin in lanes 4-9.

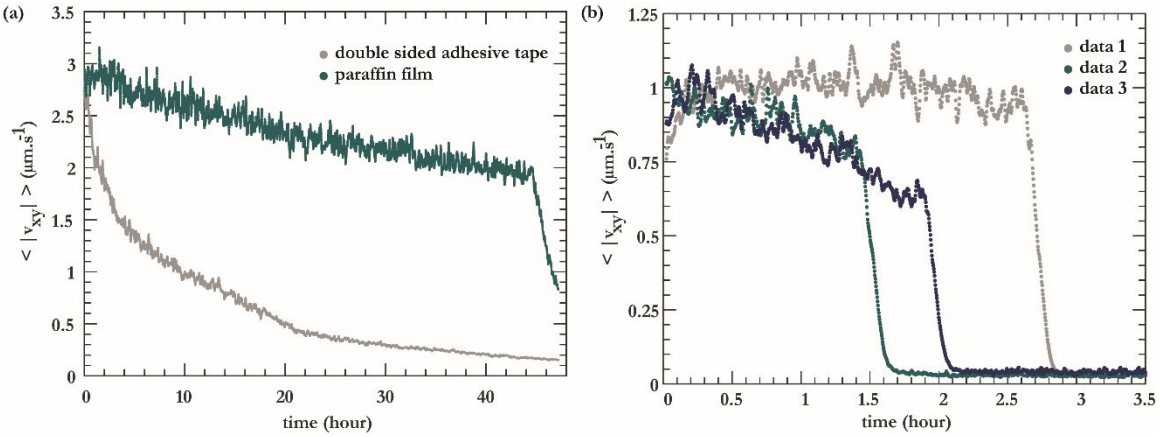

Fig. 3. Sensitivity to type of confinement and reproducibility of the active fluids. **(a)** Dynamics of the active fluid is sensitive to the chemical nature of the flow chamber. The flow chambers containing adhesive tape exhibit sample degradation, [BG-MTs = 13.3 μM, K560-SNAP = 50 nM, ATP = 1.42 mM, pluronic = 2 %]. **(b)** Reproducibility of the active fluid dynamics with three samples that are prepared independently of each other. [MTs = 13.3 μM, K401-clusters = 121 nM, ATP = 1.42 mM, pluronic = 2 %].

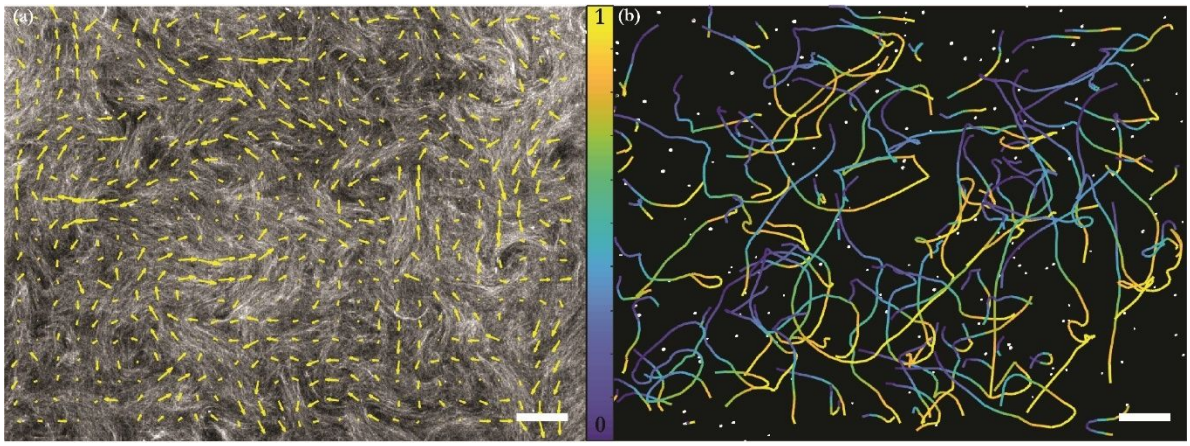

Fig.4. Large-scale flows of isotropic active fluid. (a) The flow field of active fluid is quantified by visualizing fluorescently labelled MTs; yellow arrows represent the velocity field obtained using PIV. Scale bar is 200 μm. **(b)** Trajectories of passive tracer particles (bright dots) advected by the active flows. Color bar represents the passage of time from 0 to 1 minute. Scale bar, 200 μm. [MTs = 13.3 μM, K401-clusters = 121 nM, ATP = 1.42 mM, pluronic = 2 %].

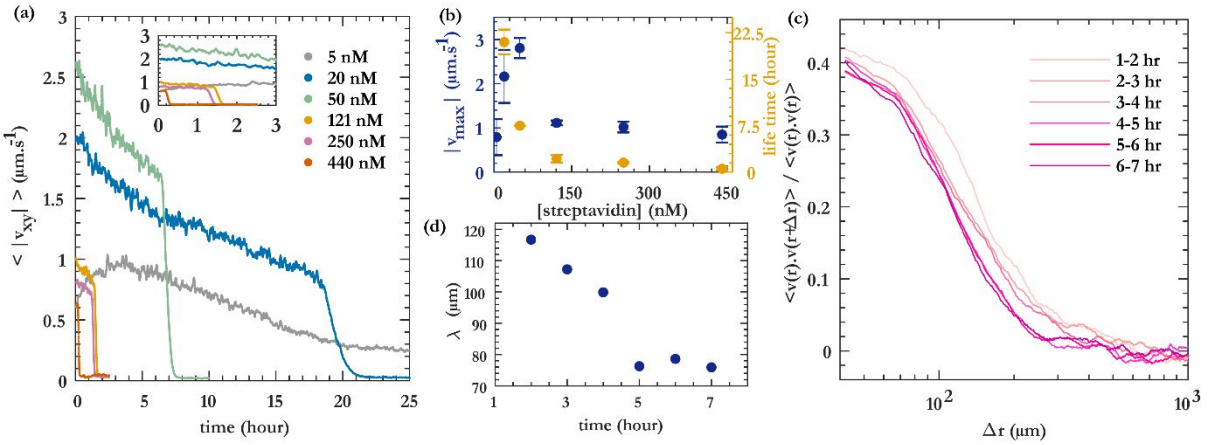

Fig.5. Active fluid powered by processive K401 motors. (a) Time dependence of the mean speed of tracer particles advected by the active fluid measured at different K401 cluster concentrations. **(b)** Maximum speed and sample lifetime for different K401 clusters concentration. **(c)** Spatial velocity-velocity correlation of tracer particles plotted as a function of particle separation, for 50 nM cluster concentration. The spatial velocity correlation is average over one hour. **(d)** Time evolution of the correlation length, λ, extracted from the spatial correlation function. [MTs = 13.3 μM, ATP = 1.42 mM, pluronic = 2 %, temperature = 20 ˚C].

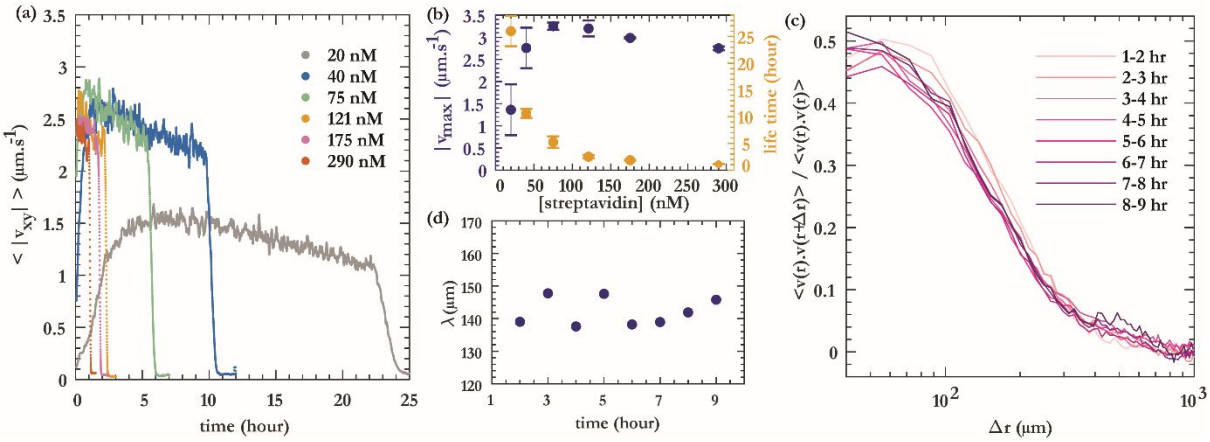

Fig.6. Active fluid powered by non-processive K365 motors. (a) Time dependence of the mean speed of active fluid at different K365 cluster concentrations. **(b)** Maximum speed of tracer paticles and the sample lifetime as a function of K365 cluster concentration. **(c)** Spatial velocity-velocity correlation of tracer particles plotted as a function of particle separation, for 50 nM cluster concentration. The spatial velocity correlation is average over one hour. **(d)** Time evolution of the correlation length, λ, extracted from the spatial correlation function. [MTs = 13.3 μM, ATP = 1.42 mM, pluronic = 2 %, temperature = 20 ˚C].

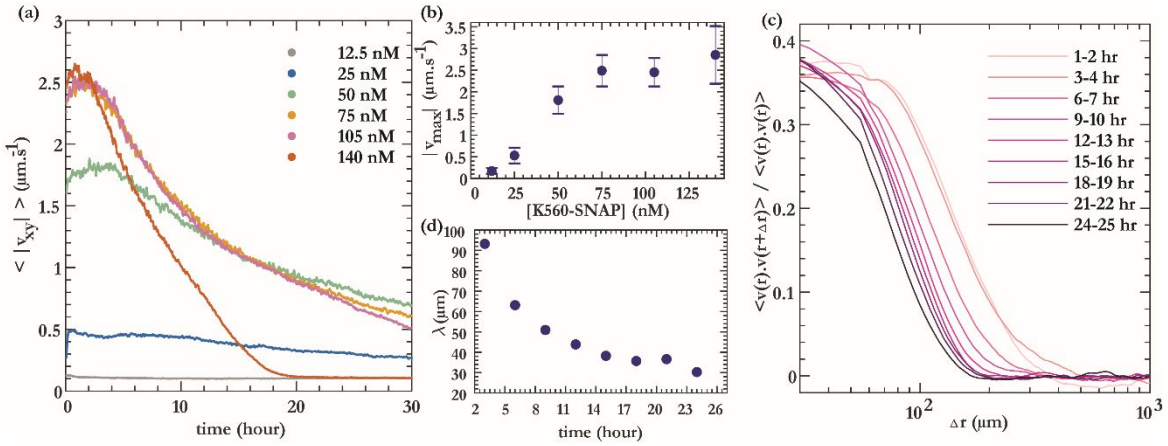

Fig. 7. Active fluid powered by K560-SNAP motors linked to BG labelled MTs. (a) Time dependence of the mean speed of tracer particles advected by the active fluid. Data is shown for different concentration of K560-SNAP. The active fluid contains only BG-MT-SNAP-K560 interactions, K560-SNAP oligomers are removed. **(b)** Maximum speed of tracer paticles and the sample lifetime as a function of K560-SNAP concentration. **(c)** Time evolution of the velocity-velocity correlation of tracer particles plotted as a function of particle separation, for 50 nM K560-SNAP concentration. The spatial velocity correlation is average over one hour. **(d)** Time evolution of the correlation length, λ, extracted from the spatial correlation function. [MTs = 13.3 μM, ATP = 1.42 mM, pluronic = 2 %, temperature = 20 ˚C].

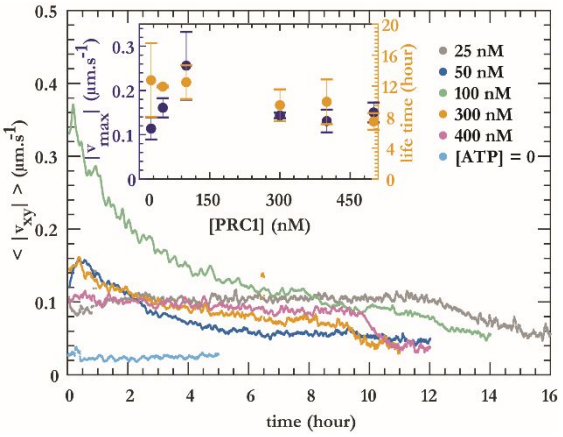

Fig. 8. Dynamics of PRC1-based active fluids. Dependence of mean speed of tracer particles on the PRC1 concentrations. Inset : maximum speed of tracer particles and the life time of the active fluid as a function of PRC1 concentration. K401 clusters (250 nM) drive the dynamics. [MTs = 13.3 μM, ATP = 1.42 mM, temperature = 20 ˚C].

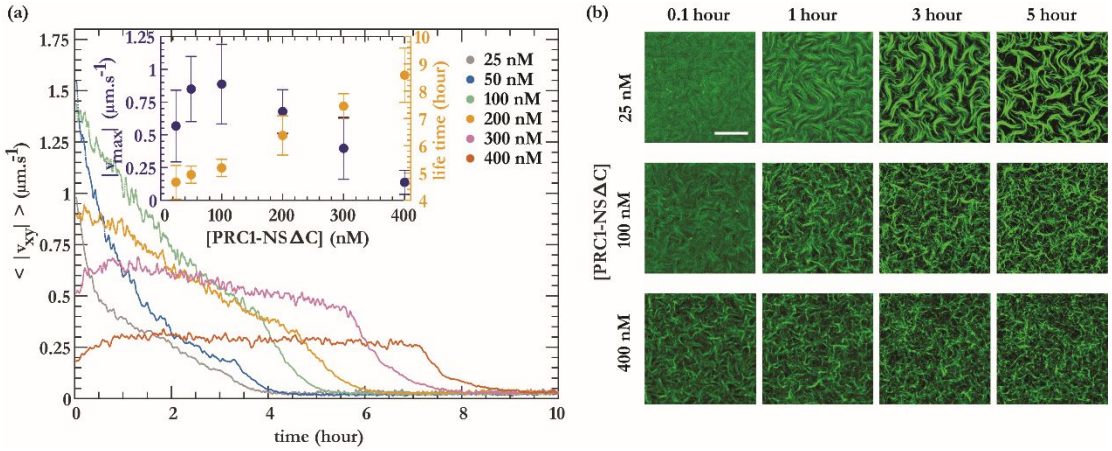

Fig. 9. Enhanced dynamics with truncated PRC1. (a) Dependence of mean speed of tracer particles on the PRC1-NSΔC concentrations. Inset: Dependece of maximum speed and the fluid lifetime on PRC1-NSΔC concentration. **(b)** Structure of active fluids consisting of different amounts of PRC1-NSΔC observed with fluorescence microscopy. K401 clusters (250 nM) drive the dynamics. Images taken with fluorescence microscope. Scale bar, 500 μm. [MTs = 13.3 μM, ATP = 1.42 mM, temperature = 20 ˚C].